Advanced Materials

ADVANCED MATERIALS
www.advmat.de

RESEARCH ARTICLE

Tailored Surface Microenvironment of Molecular Nanophotocatalysts for Boosting Photocatalytic Hydrogen Evolution

Xueyan Liu[1] | Ke Wang[2] | Haiyang Huang[1] | Miaojie Yu[1] | Chao Li[3] | Chengyang Jiang[1] | Hongxu Gu[1] | Jing Qi[1] | Guowei Shi[1] | Long Hu[1] | Fuxing Chu[1] | Shiqiang Cheng[1] | Kunchi Xie[2] | Xiaobo Li[4] | Teng-Teng Chen[3] | Yongzhen Wu[1,5] | Zhen Song[2] | Wei-Hong Zhu[1,5] | Weiwei Zhang[1,5]

[1]State Key Laboratory of Green Chemical Engineering and Industrial Catalysis, Key Laboratory for Advanced Materials and Institute of Fine Chemicals, Shanghai Key Laboratory of Functional Materials Chemistry, Center of Photosensitive Chemicals Engineering, Feringa Nobel Prize Scientist Joint Research Center, School of Chemistry and Molecular Engineering, East China University of Science and Technology, Shanghai, China | [2]State Key Laboratory of Chemical Engineering and Low-Carbon Technology, School of Chemical Engineering, East China University of Science and Technology, Shanghai, China | [3]Department of Chemistry, The Hong Kong University of Science and Technology, Kowloon, Hong Kong, P. R. China | [4]State Key Laboratory of Precision and Intelligent Chemistry, University of Science and Technology of China, Hefei, Anhui, China | [5]Guangxi Laboratory of Low-Carbon Technology and Green Chemical Advanced Materials, Qinzhou, Guangxi, China

Correspondence: Zhen Song (songz@ecust.edu.cn) | Wei-Hong Zhu (whzhu@ecust.edu.cn) | Weiwei Zhang (zhangweiwei@ecust.edu.cn)

Received: 2 April 2026 | **Revised:** 29 May 2026 | **Accepted:** 25 June 2026

Keywords: organic nanophotocatalysts | photocatalytic hydrogen evolution | surface microenvironment | surfactants

ABSTRACT

Organic photocatalysts are an attractive platform for solar-to-chemical energy conversion, but their performance is often constrained by bulk aggregation, poor light penetration, and rapid exciton recombination. Although surfactant-assisted nanostructuring can help alleviate aggregation, surfactants are generally treated as passive stabilizers with little direct influence on photocatalytic function. Here we show that surfactants can actively engineer the interfacial microenvironment of organic nanophotocatalysts, leading to substantially enhanced photocatalytic hydrogen evolution. A donor–acceptor small molecule, CNP90, is co-assembled with either hydrophilic polyethylene glycol (PEG) or amphiphilic Tween surfactants (Tween 20, T20; Tween 80, T80) via nanoprecipitation to afford a series of tailored nanophotocatalysts. Although all surfactants improve colloidal stability, T20/CNP90 exhibits markedly enhanced photoluminescence quantum yield and charge generation, leading to a more than 16-fold increase in the hydrogen evolution rate to 520.17 mmol g^{-1} h^{-1}, among the highest values reported for organic photocatalysts. Spectroscopic studies combined with molecular dynamics simulations reveal that T20 constructs an amphiphilic interfacial microenvironment around CNP90, comprising a hydrophobic inner shell that suppresses nonradiative recombination and a hydrophilic outer corona that promotes water access to catalytic sites. These insights establish surfactant-driven microenvironment engineering as a powerful, low-cost, and generalizable paradigm for maximizing the performance of organic photocatalysts.

Xueyan Liu, Ke Wang and Haiyang Huang contributed equally to this work.

1 | Introduction

The escalating global demand for sustainable and renewable energy has intensified efforts to develop advanced strategies for solar-to-chemical conversion [1–6]. Photocatalytic solar fuel production, which directly harnesses sunlight to drive chemical transformations, has emerged as a promising route to alleviate energy shortages and mitigate environmental challenges [7–11]. Within this landscape, organic photocatalysts have attracted considerable attention as a versatile class of light-harvesting materials [7, 12–21]. Their strong visible-light absorption, highly tunable band structures, and molecular design flexibility enable precise control of optical and physical properties to meet specific reaction requirements [21, 22]. Representative materials include covalent organic frameworks (COFs), conjugated polymers, and molecular assemblies [22–28]. Despite these advantages, organic photocatalysts are often synthesized as microscale bulk aggregates due to the typical use of large aromatic building blocks and, in some cases, poorly controlled polymerization processes [22, 23, 29, 30]. Such large particles can result in substantial losses in light harvesting and exciton utilization, since light penetration depths in organic semiconductors are typically limited to a few hundred nanometers, while exciton diffusion lengths are often below 50 nm [31–34]. These intrinsic mismatches severely constrain the photocatalytic performance [31, 32].

Nano-structuring organic materials into colloidal nanoparticles is a recognized strategy to mitigate these issues by shortening exciton migration distances to reactive interfaces, increasing the exposure of active sites, and improving photocatalytic performance [35–42]. However, because most organic semiconductors are inherently hydrophobic and prone to re-aggregation in aqueous media, it is necessary to impart sufficient hydrophilicity to obtain stable nanoparticulate photocatalysts. This is commonly achieved through main-chain or side-chain engineering of the molecular building blocks [26, 43–45]. While effective, such structural modifications often rely on complex, multistep synthetic routes that are labor-intensive and time-consuming, and may perturb intermolecular packing, limiting scalability and reproducibility [46]. On the other hand, surfactant-assisted solution processing, via mini-emulsion or nanoprecipitation, offers a simpler, broadly applicable route to fabricate nanophotocatalysts while preserving their intrinsic electronic properties. In these processes, surfactants play an essential role as stabilizers during nanoparticle formation [47–49]. Nevertheless, the influence of surfactants on photocatalytic activity remains quite controversial. The prevailing practice is to remove surfactants after synthesis, based on the assumption that insulating surface layers hinder interfacial charge transfer [50–52]. In contrast, several studies revealed that surfactants can enhance photocatalytic performance by improving surface hydrophilicity or facilitating cocatalyst loading [40]. This apparent dichotomy highlights a critical knowledge gap, as the mechanistic roles of surfactants at the catalyst–solution interface remain poorly understood.

Here, we address this controversy by constructing molecular nanophotocatalysts with distinct surfactants and systematically elucidating their effects on photophysical behavior and photocatalytic hydrogen evolution. Specifically, a donor–acceptor (D–A) small molecule, 2,6-bis(4-cyanophenyl)-4-(9-phenyl-9H-carbazol-3-yl) pyridine-3,5-dicarbonitrile (CNP90), was nanoprecipitated with either polyethylene glycol (PEG; hydrophilic polymer) or the amphiphilic surfactants Tween 20 (T20) and Tween 80 (T80, featuring longer hydrophobic chains) via solution processing (Figure 1a). Compared with bare CNP90 assemblies, incorporation of PEG or Tween can markedly improve colloidal stability and dispersion without significantly perturbing the molecular packing of the CNP90 core. Interestingly, we found that T20 induces the formation of an amphiphilic interfacial microenvironment on CNP90, in which the hydrophobic alkyl chain of T20 protects the organic core of CNP90 from the aqueous environment, suppressing its nonradiative recombination loss, while the hydrophilic polyoxyethylene strengthens the water–catalyst interfacial layer by modulating the hydrogen-bonding network. This synergistic microenvironment engineering led to more than a 16-fold enhancement in the hydrogen evolution rate (HER), relative to bare CNP90, achieving a HER of 520.17 mmol g^{-1} h^{-1} under visible light irradiation, which surpassed most reported organic photocatalysts. These findings uncover the critical role of surfactant-induced interfacial microenvironment regulation in organic nanophotocatalysts and establish a general and facile strategy for enhancing photocatalytic performance.

2 | Results and Discussion

2.1 | Constructing D-A Structured Molecular Nanophotocatalysts with Surfactants

Tween (polyoxyethylene sorbitan monolaurate) is an amphipathic surfactant widely used in nanomaterial synthesis, which consists of a hydrophobic fatty acid chain and hydrophilic polyoxyethylene segments. Here, we selected Tween 80 (C_{18} oleate, T80) and Tween 20 (C_{12} laurate, T20), which differ in hydrophobic chain length, for nanoparticle synthesis together with a donor–acceptor (D–A) structured small molecule, CNP90 (Figure S28). For comparison, a fully hydrophilic polymer, polyethylene glycol (PEG), was included as a reference. For preparing the nanophotocatalysts, CNP90 was dissolved in acetone, while T80, T20, or PEG was dissolved separately in water. The CNP90 solution was then added dropwise into the surfactant or PEG solution under continuous stirring, and the acetone solvent was subsequently removed at elevated temperature (80°C). We note that all as-synthesized samples, including bare CNP90, formed uniform colloidal dispersions, exhibiting a clear Tyndall effect (Figure 1b, inset). Zeta potential measurements showed similar values of approximately −20 mV for all nanoparticles. However, after one month of storage, bare CNP90 and PEG/CNP90 displayed visible aggregation and sedimentation, while the samples containing T80 or T20 remained clear and stable with no significant change in zeta potential.

To investigate the nanoparticle composition, the samples were isolated and then subjected to vacuum dried. Fourier-transform infrared (FT-IR) spectra exhibited a prominent absorption band at approximately 2229 cm^{-1} for all samples, corresponding to the characteristic C≡N stretching vibration of CNP90 (Figure 1c). In the PEG/CNP90 system, although neat PEG exhibits $-CH_2-$ stretching vibrations at ∼ 2860 and 2884 cm^{-1}, these PEG signatures were absent from the FT-IR spectrum of the PEG/CNP90 assemblies after extensive rinsing (Figure S1), indicating a weak association between PEG and the CNP90. In contrast, the

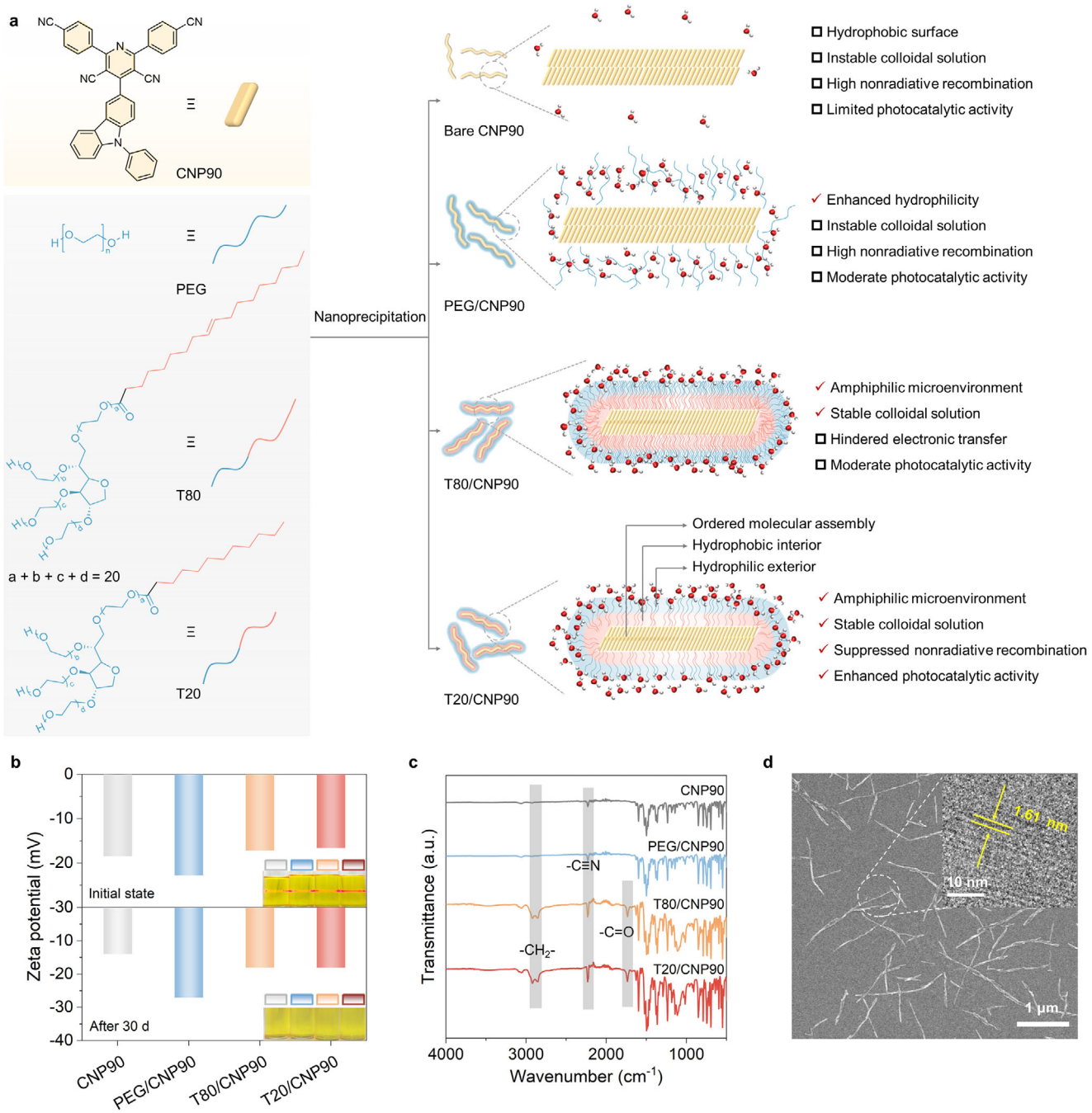

FIGURE 1 | Synthesis of CNP90 nanofiber with different surfactants. (a) Schematic illustration of the surfactant-assisted nanoprecipitation for constructing CNP90-based supramolecular assemblies. CNP90 was co-assembled with PEG, T80, or T20 to generate nanophotocatalysts with different core–shell structures. (b) Zeta potentials of CNP90, PEG/CNP90, T80/CNP90, and T20/CNP90 colloidal dispersions, measured immediately after preparation and after 30 days of storage; insets show the corresponding digital photographs. (c) Fourier-transform infrared (FTIR) spectra of CNP90, PEG/CNP90, T80/CNP90, and T20/CNP90 assemblies obtained by filtration. (d) Scanning electron microscopy (SEM) image of T20/CNP90 nanofibers showing the fiber-like morphology; inset shows cryogenic transmission electron microscopy (cryo-TEM) images and high-resolution lattice fringes of T20/CNP90 nanofibers.

characteristic carbonyl stretching vibration at 1721 cm^{-1}, originating from T80 and T20, persisted in the spectra of T80/CNP90 and T20/CNP90 after washing, accompanied by the methylene symmetric and asymmetric stretching vibrations at 2852 and 2922 cm^{-1}, respectively. The coexistence of these signature peaks suggested the co-assembly of T20 and T80 with CNP90, and their stronger association with the CNP90 nanofibers relative to PEG.

The morphology of these nanofibers was characterized by scanning electron microscopy (SEM; Figure 1d and Figure S2) and scanning transmission electron microscopy (STEM; Figure S3). All samples exhibited similar fibrous morphologies. Compared to bare CNP90 nanofibers, the introduction of the PEG or Tween slightly reduced the average fiber length, as well as the average height (Figure S4). Cryogenic transmission electron

microscopy (cryo-TEM) images (insets of Figure 1d) revealed well-defined lattice fringes within the nanofibers, with similar interplanar spacings of 1.58 and 1.61 nm for CNP90 and T20/CNP90, respectively. These values are consistent with the powder X-ray diffraction (PXRD) patterns of the freeze-dried samples (Figure S5; $2\theta \approx 5.8°$), indicating that the presence of the surfactant does not significantly alter the crystalline assembly of CNP90.

2.2 | Boosted Photocatalytic Hydrogen Evolution Rate with T20

Photocatalytic experiments were carried out in aqueous solutions, using in situ photo-deposited platinum (Pt) as a cocatalyst, and ascorbic acid (AA) as the sacrificial agent (Figure S9). As shown in Figure 2a, under visible light irradiation (> 420 nm), bare CNP90 nanophotocatalysts produced 243.8 μmol of H_2 in 5 h, corresponding to a hydrogen evolution rate (HER) of 48.8 μmol h^{-1}. In comparison, introducing the hydrophilic polymer PEG led to a modest improvement, yielding 462.9 μmol of H_2 over the same period. Notably, replacing PEG with the amphipathic surfactant T20 resulted in a greatly enhanced H_2 production of 3901.3 μmol, corresponding to a HER of 780.3 μmol h^{-1}. However, nanoprecipitation with T80, which possesses a longer hydrophobic chain, led to a slight decrease in hydrogen production (2504.1 μmol, 500.8 μmol h^{-1}). These results suggest that the surfactants for nonprecipitation can profoundly influence photocatalytic performance.

The concentration of T20 was found to influence photocatalytic activity as well. The HER exhibited a distinct volcano-type dependence on T20 concentration (Figure 2b). Specifically, increasing the surfactant concentration from 0 to 0.5 mg mL^{-1} led to a marked enhancement in hydrogen production, reaching 823.5 μmol h^{-1} at 0.5 mg mL^{-1}. This gradual improvement in photocatalytic activity can be attributed to the enhanced encapsulation of CNP90 by T20, which shields CNP90 from the polar aqueous environment and thereby suppresses nonradiative recombination, as discussed below. Beyond this optimal point, however, the HER gradually declined to 135.6 μmol h^{-1} at 10 mg mL^{-1}. This decline is likely due to the excessively high T20 concentration, which forms an overly dense surfactant layer around CNP90, hindering reactant transport, such as sacrificial donors and water, and suppressing interfacial charge transfer. Under optimized conditions (1.5 mg CNP90 and 8 wt.% Pt; Figure S7), T20/CNP90 nanofibers produced 3901.3 μmol H_2 within 5 h, corresponding to a mass-normalized HER of 520.17 mmol g^{-1} h^{-1}—a 16-fold enhancement relative to bare CNP90 (32.51 mmol g^{-1} h^{-1}). Under simulated one-sun illumination (AM 1.5G, 100 mW cm^{-2}), the T20/CNP90 nanofibers also delivered a high HER of 244.44 mmol g^{-1} h^{-1} (Figure S8). To the best of our knowledge, these HERs exceed those of most reported organic photocatalysts, underscoring the critical role of surfactants in enhancing photocatalytic performance.

The apparent quantum yield (AQY), reflecting the efficiency of converting incident photons into hydrogen, was determined for the optimized T20/CNP90 nanofibers. The AQYs at 400, 420, 450, and 500 nm (Figure 2c) were calculated to be 22.34%, 10.41%, 9.73%, and 0.80%, respectively. These values highlight the effective light harvesting and charge utilization of T20/CNP90 across the UV–visible spectrum. The long-term stability of the system was evaluated over seven consecutive photocatalytic cycles (5 h each) under continuous visible-light irradiation (Figure 2d). Bare CNP90 were found to show rapid decline, accompanied by pronounced particle aggregation (Figure S10), whereas T20/CNP90 maintained nearly constant activity over at least 35 h. These results indicate that nanoprecipitation with amphipathic surfactant T20 not only enhances photocatalytic activity but also improves operational stability. After the photocatalytic reaction, FTIR, X-ray photoelectron spectroscopy (XPS), SEM, and TEM analyses confirmed that T20/CNP90 retained its chemical structure and morphology (Figures S11–S15), further supporting its robust photostability.

We compare the photocatalytic performance of T20/CNP90 against some representative literature-reported photocatalysts using five critical metrics: mass-normalized hydrogen evolution rate, photocatalyst dosage, hourly hydrogen productivity, apparent quantum yield, and long-term stability (Figure 2e). T20/CNP90 demonstrates comparable or superior performance across all categories, most notably achieving high hydrogen output at very low catalyst loadings. This contrasts with previous studies, where high mass normalized HER values for nanophotocatalysts were typically obtained only at low catalyst dosages, resulting in limited overall productivity.

To minimize comparability issues arising from variations in testing conditions across laboratories, we also benchmarked the photocatalytic activity of T20/CNP90 against some state-of-the-art organic photocatalysts under our experimental platform, including F8BT, P3HT:$PC_{71}BM$, PM6:$PC_{71}BM$, RC-COF-1, and perylenetetracarboxylic acid (PTA) nanosheets (see Supporting Information for details). These reference photocatalysts showed activities comparable to their literature values, whereas T20/CNP90 significantly outperformed these photocatalysts (Figure 2f).

To assess the scalability of the champion nanophotocatalysts T20/CNP90, a flash nanoprecipitation (FNP) technique was employed for continuous flow synthesis [41] (Figure S16a). This process enables facile scale-up of production, achieving a space–time yield of 6 L h^{-1}. As shown in Figure 2g, the FNP-produced nanophotocatalysts demonstrated photocatalytic activity parallel to that of stirring-based batch synthesis, achieving a remarkable HER of 536.37 mmol g^{-1} h^{-1}. Furthermore, owing to the excellent stability and dispersibility of the resulting colloidal dispersion, they can be readily deposited onto nylon membranes. These films delivered an outstanding hydrogen production rate of 483.83 mmol m^{-2} h^{-1} as well (Figure 2h), representing a 14-fold enhancement compared with films prepared from bare CNP90. These results suggested that the strategy is readily translatable to film-based devices.

Motivated by the pronounced enhancement in photocatalytic activity achieved through T20-assisted nanoprecipitation, we further evaluated the generality of this strategy across a range of molecular and polymeric photocatalysts. A series of well-established organic photocatalysts, including CNP, NPI, F8BT, 4CzPN, and $PC_{71}BM$, were individually co-precipitated with T20. In all cases, the HER was found to substantially improve, with

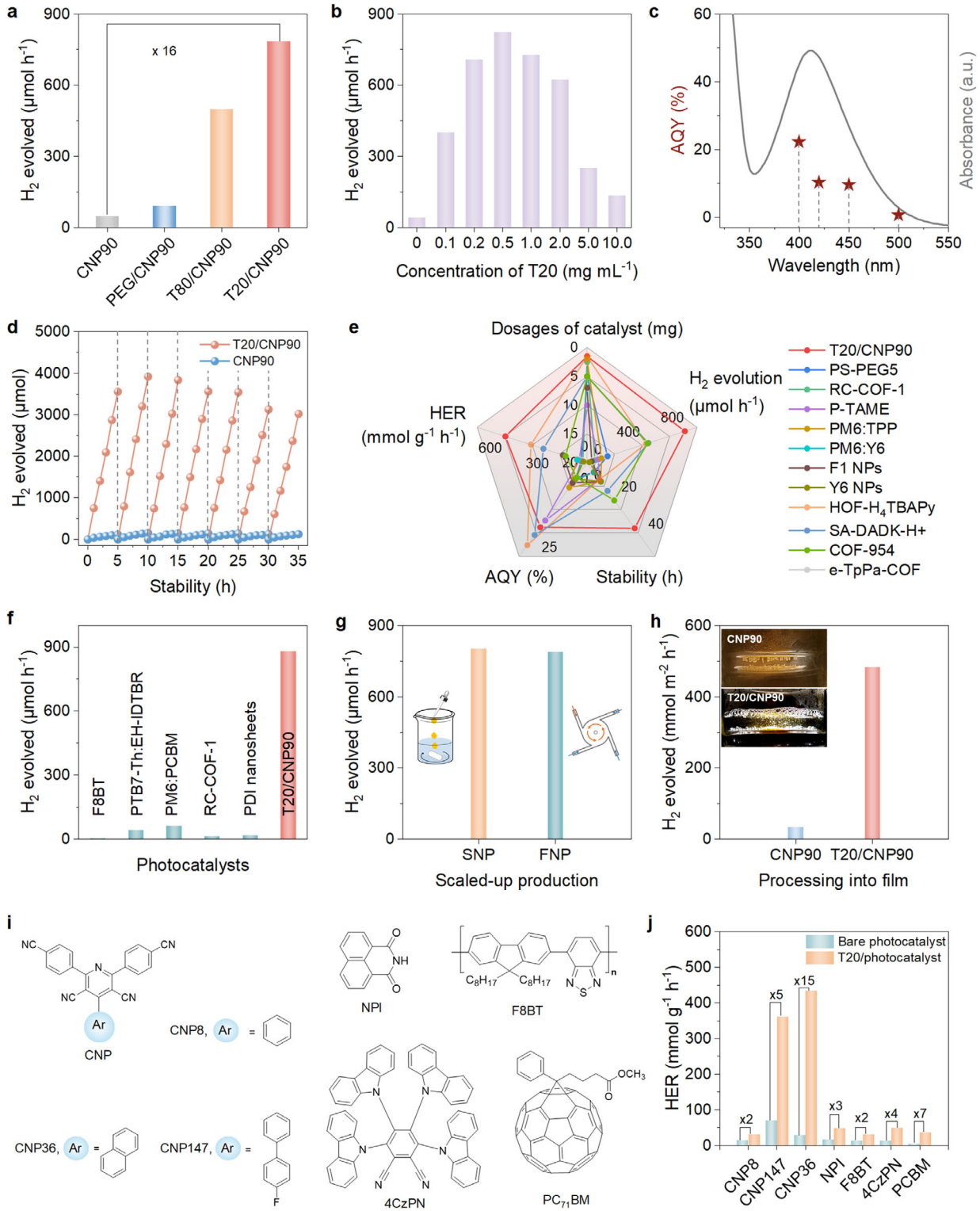

FIGURE 2 | Photocatalytic hydrogen evolution performance. (a) Comparison of photocatalytic hydrogen evolution for CNP90, PEG/CNP90, T80/CNP90, and T20/CNP90 nanofibers (1.5 mg photocatalyst, 25 mL H_2O, 0.20 M ascorbic acid, and 8 wt.% Pt as cocatalyst relative to CNP90). (b) Hydrogen evolution of T20/CNP90 nanofibers synthesized with different T20 concentrations. (c) AQYs of the optimized T20/CNP90 nanophotocatalysts measured at excitation wavelengths of 400, 420, 450, and 500 nm, respectively. (d) Long-term photocatalytic hydrogen evolution stability of T20/CNP90 under visible-light irradiation (ascorbic acid replenished every 5 h). (e) Radar plot comparing photocatalytic performance metrics, including catalyst dosage, hydrogen evolution rate, stability, AQY, and overall HER. (f) Experimental comparison of hydrogen evolution activities of some state-of-the-art organic photocatalysts. (g) Hydrogen evolution performance of T20/CNP90 synthesized via stirring nanoprecipitation (SNP) and flash nanoprecipitation (FNP) methods. (h) Hydrogen evolution performance of a circular photocatalyst film (diameter: 4 cm) prepared from the colloidal solution. (i,j) Photocatalytic hydrogen evolution across various organic photocatalysts. Detailed experimental procedures are provided in the Supporting Information methods.

enhancement factors ranging from 2- to 15-fold (Figure 2i). These results highlight the broad applicability of T20-assisted nanoprecipitation as an effective strategy for constructing highly active nanophotocatalysts.

2.3 | Decreased Nonradiative Recombination Loss and Enhanced Charge Generation

To evaluate how co-precipitation with surfactants affects the performance of nanophotocatalysts, the water contact angles were measured on the films fabricated from these nanocomposites. As shown in Figures 3a and S6, bare CNP90 exhibited a water contact angle of ~70°, which decreased to 13°, 33°, and 8° for PEG/CNP90, T80/CNP90, and T20/CNP90, respectively, indicating a pronounced enhancement in surface hydrophilicity. In line with this trend, T20/CNP90 showed more than a twofold increase in water uptake compared to CNP90. The optical properties of these colloidal dispersions were studied using UV–vis absorption spectroscopy (Figure 3b). All samples exhibited a characteristic charge-transfer (CT) absorption band centered at approximately 415 nm, primarily associated with electron donation from the carbazole moiety to the cyano-substituted pyridine acceptor in CNP90. Given that the nanofibers are assembled from ordered CNP90 molecules, this absorption band likely contains contributions from both intramolecular and intermolecular charge-transfer interactions. PEG/CNP90, T80/CNP90, and T20/CNP90 exhibited slightly higher absorbance than bare CNP90, which can be attributed to improved nanofiber dispersion due to the incorporation of hydrophilic polymer or amphiphilic surfactants. This interpretation is supported by the photographic inserts, in which PEG/CNP90, T80/CNP90, and T20/CNP90 display superior colloidal stability and optical transparency (Figure 3b). The optical bandgaps of these nanophotocatalysts are estimated to be ~2.5 eV from their absorption onsets (Figure S17). Mott–Schottky (M–S) analysis (Figure S18) was employed to determine the conduction band positions, which revealed a relatively negative conduction band that are theoretically energetic to drive proton reduction (Figure S19 and Table S1).

Photoluminescence (PL) spectroscopy was performed to probe the excitonic properties of these nanocomposites (Figure 3c). Under 405 nm excitation, pristine CNP90 exhibited weak emission centered at 663 nm, while PEG/CNP90 showed a slight increase in PL intensity, consistent with its improved absorbance. Remarkably, T80/CNP90 and T20/CNP90 exhibited ~4-fold increases in PL intensity, respectively. In general, PL emission primarily reflects the efficiency of radiative recombination of singlet excitons and is influenced by molecular packing and microenvironment. Considering CNP90, T80/CNP90, and T20/CNP90 show similar crystallinity, the pronounced enhancement in the surfactant-encapsulated samples likely arises from suppression of nonradiative decay channels. To validate this, we quantified radiative efficiency using photoluminescence quantum yield (PLQY) measurements (Figure 3d). Different from PL intensity, which depends on sample concentration, optical path length, and instrumental settings, PLQY provides an absolute measure of the fraction of absorbed photons re-emitted as fluorescence. The measured PLQYs followed the same trend as the steady-state PL spectra, with values of 1.2% (CNP90), 1.5% (PEG/CNP90), 2.6% (T80/CNP90), and 3.1% (T20/CNP90). Time-correlated single-photon counting (TCSPC) analysis was conducted to explore the excited-state decay processes. By fitting with a triexponential decay function, the average PL lifetime of CNP90 nanofibers was calculated to be 6.34 ns, and it increased to 16.00 and 14.12 ns for the T80/CNP90 and T20/CNP90, respectively (Figure 3e, Figure S20 and Table S2). These results indicate that interactions between the Tween and nanoparticles could enhance fluorescence by suppressing nonradiative exciton recombination, attributable to the formation of a surfactant-induced hydrophobic microenvironment on the CNP90 surface (discussed later).

Transient absorption spectroscopy (TAS) was employed to monitor the evolution of photoexcited species. The characteristic absorption band centered at ~870 nm is attributed to the charge-transfer (CT) state [38]. In the presence of ascorbic acid (AA), notably, the T20/CNP90 composite exhibits more than a two-fold increase in CT signal intensity compared to pristine CNP90, indicative of a substantially enlarged CT-state population (Figure 3f–h). This enhanced CT signal is expected to promote the generation of a greater number of polarons in the T20 modulated system, facilitating the photocatalytic hydrogen evolution reaction. To further probe the charge-generation properties, electron paramagnetic resonance (EPR) spectroscopy was performed using TEMPO as a spin probe. The initial TEMPO spectrum, which displays a well-resolved three-line pattern with resonance fields at 3352, 3370, and 3388 G, was recorded as the baseline. Upon illumination, photogenerated electrons from the nanophotocatalysts can reduce TEMPO, leading to quenching of its EPR signal; thus, the extent of TEMPO quenching reflects the efficiency of charge-carrier generation (Figure S22). As shown in Figure 3i, CNP90 and PEG/CNP90 displayed only minor signal quenching after 5 min of light irradiation, whereas T20/CNP90 and T80/CNP90 exhibited substantially stronger quenching, suggesting that incorporating T20 or T80 markedly increases electron generation. These results are further corroborated by photoelectrochemical measurements: photocurrent responses and electrochemical impedance spectra indicated that T20/CNP90 and T80/CNP90 films produced higher photocurrents and lower charge-transfer resistance than bare CNP90 (Figure S21), confirming the enhanced photoinduced charge generation.

2.4 | Engineered Microenvironment with a Hydrophilic Exterior and Hydrophobic Interior

Surface microenvironment, which refers to the local physicochemical conditions in the immediate vicinity of a photocatalyst, including local polarity, hydrophilicity/hydrophobicity, water/reactant concentration, and interfacial accessibility, can strongly influence exciton recombination, charge-carrier generation, and reactant transport in organic nanophotocatalysts [53, 54]. To gain molecular-level insight into the cooperative interactions between CNP90 and different surfactants, molecular dynamics (MD) simulations were performed to investigate their assembly configurations and structural evolution. Four model systems were constructed: bare CNP90, CNP90 co-assembled with PEG2000, T20, or T80, respectively (Figures 4a and S23a). Interestingly, the T20/CNP90 system adopts a core–shell architecture, in which an ordered CNP90 assembly forms the inner

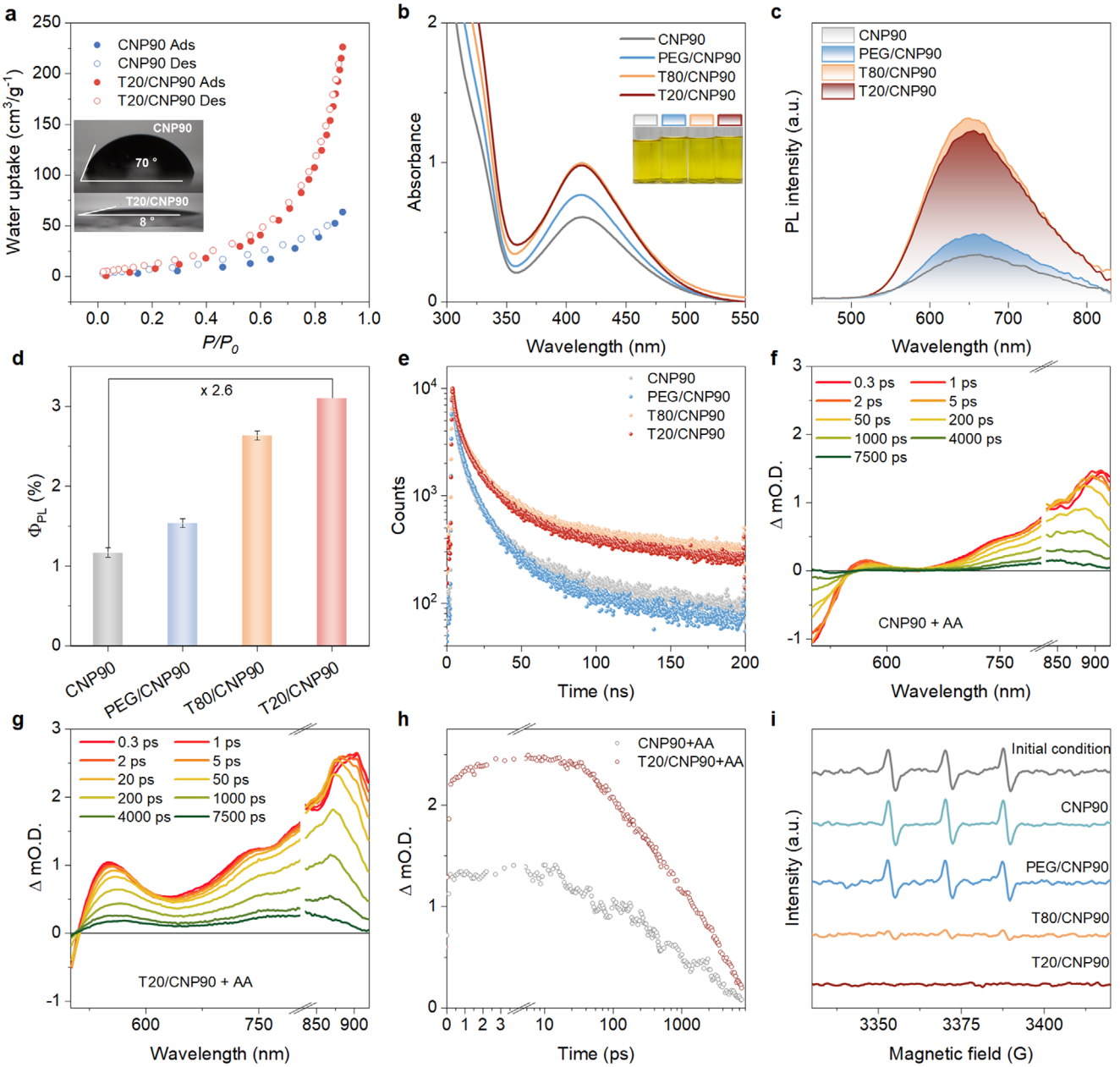

FIGURE 3 | Photophysical and photochemical properties of nanophotocatalysts. (a) Water adsorption–desorption isotherms for CNP90 and T20/CNP90 measured at 298 K; insets show the corresponding water contact angles. (b–e) UV–vis absorption spectra (b), steady-state photoluminescence (PL) spectra (c, λ_{exc} = 405 nm), photoluminescence quantum yields (PLQY) (d, λ_{exc} = 405 nm), and time-resolved photoluminescence (TRPL) spectra (e, λ_{exc} = 405 nm) of CNP90, PEG/CNP90, T80/CNP90, and T20/CNP90. (f, g) Deconvoluted transient absorption kinetics of CNP90 and T20/CNP90 under 405 nm excitation in the presence of ascorbic acid (AA). (h) Deconvoluted transient absorption kinetics of CNP90 (probe wavelength 870 nm) and T20/CNP90 (probe wavelength 885 nm). (i) Comparison of changes in EPR signal intensity of TEMPO upon addition of CNP90, PEG/CNP90, T80/CNP90, and T20/CNP90 photocatalysts after 5 min of light illumination.

core, while T20 molecules adsorb onto the nanofiber surface to create the outer shell. In this configuration, the hydrophobic alkyl chains of T20 preferentially orient toward the CNP90 core, whereas the hydrophilic poly (ethylene oxide) segments extend into the surrounding aqueous phase. This arrangement is analogous to the micellar structure of T20, as the T20 concentration is well above its critical micelle concentration (CMC, 0.06 mM in water). In particular, the hydrophobic alkyl chain of T20 has a strong affinity for the aromatic rings of CNP90, thereby facilitating the encapsulation of CNP90 within the micellar core. This amphiphilic organization leads to a pronounced accumulation of water molecules at the outer surface of the assembly, along with a dense hydrogen-bonding network at the interface. By contrast, the PEG/CNP90 system does not achieve complete or uniform encapsulation of the CNP90 assemblies, likely due to the fully hydrophilic nature of PEG, which possesses weaker affinity toward CNP90.

Spatial distribution analysis of water molecules reveals distinct local hydration environments in these systems (Figure 4b and

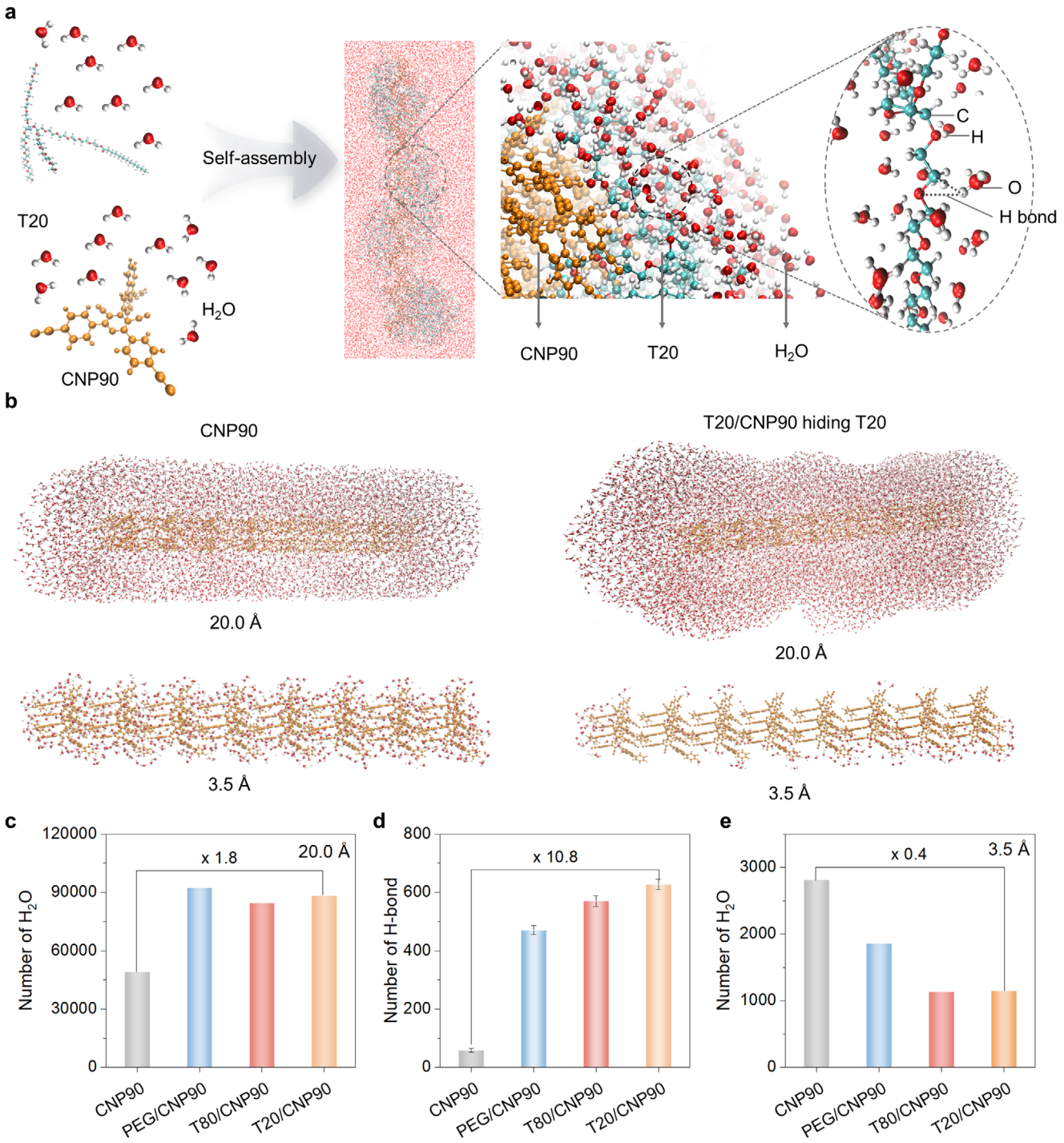

FIGURE 4 | Molecular dynamics simulations. (a) Workflow of molecular dynamic simulations. The simulation box was filled with water molecules in an amorphous cell to evaluate hydration and hydrogen-bonding behavior. (b) Left: spatial distributions of water molecules within 3.5 and 20.0 Å of the CNP90 assemblies. Right: spatial distributions of water molecules within 3.5 Å of the CNP90 core and within 20.0 Å of the T20/CNP90 composite. (c) Quantitative analysis of water molecules within a 20.0 Å radius of pristine CNP90 and its assemblies (PEG/CNP90, T80/CNP90, and T20/CNP90). (d) Quantitative analysis of hydrogen bonds of CNP90, PEG/CNP90, T80/CNP90, and T20/CNP90 assemblies. (e) Quantitative analysis of the number of water molecules within a 3.5 Å radius of pristine CNP90 and the corresponding PEG/CNP90, T80/CNP90, and T20/CNP90 assemblies.

Figure S23b). Compared to bare CNP90, co-assembly with PEG or Tween results in a substantial increase in water density in the outer region (within ~20 Å of the composite). Quantitative analysis (Figure 4c) shows that the number of water molecules in this region is nearly doubles, indicating that an enhanced water accumulation around CNP90. Further examination of the hydrogen-bonding network within the hydration layer shows that the number of hydrogen bonds increases by factors of 8.1, 9.8, and 10.8 for PEG/CNP90, T80/CNP90, and T20/CNP90, respectively, relative to pristine CNP90. These results demonstrate that co-assembly not only enriches interfacial water content but also reorganizes the hydrogen-bonding network at the catalyst

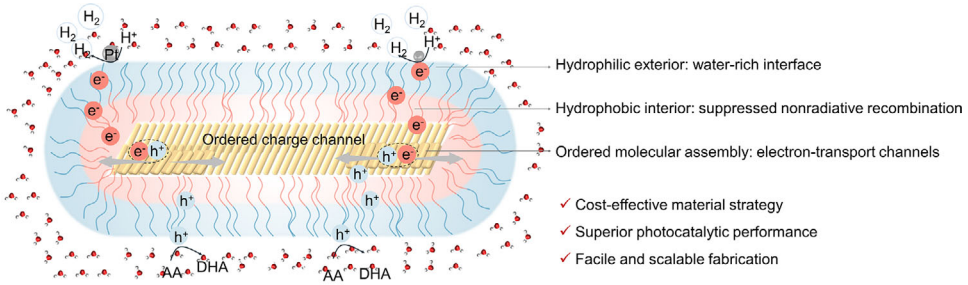

FIGURE 5 | Schematic illustration of the T20/CNP90 nanophotocatalysts with a hydrophilic exterior and a hydrophobic interior for boosting hydrogen evolution.

surface, both of which are likely to contribute to the enhanced hydrogen evolution activity by facilitating the interfacial mass transfer process (Figure 4d).

In contrast to the outer region, interestingly, the co-assembled systems showed a pronounced depletion of water in the inner region (≤3.5 Å) relative to pristine CNP90 (Figure 4b). This effect is particularly prominent in the Tween-based assemblies, where the number of internal water molecules decreases by approximately 60% for T20/CNP90 (Figure 4e). These results indicate that introducing T20 generates a hydrophobic inner microenvironment that excludes water from the CNP90 nanofiber surface. Such hydrophobic confinement provides a plausible explanation for the enhanced photoluminescence observed in Figure 3c.

Typically, excited states in organic semiconductors undergo three competing pathways: radiative recombination, nonradiative recombination, and charge separation for photocatalysis [55, 56]. For D-A molecules, polar media can strongly solvate the charge-transfer excited state, enhancing the solvent screening effect and reaction field, which accelerates electron transfer and promotes nonradiative recombination [57]. In protic solvents such as water, excited molecules can also form hydrogen-bonded complexes with surrounding water molecules, facilitating the dissipation of excitation energy into solvent vibrational modes and further enhancing nonradiative decay [58–60]. Herein, the hydrophobic microenvironment created by T20 shields CNP90 from polar water, weakens charge-transfer-state solvation, and suppresses water-mediated hydrogen-bonding interactions. Consequently, nonradiative recombination is effectively inhibited, allowing more excitons and excited-state energy to contribute to light emission and charge generation. To further validate this interpretation, PL measurements were conducted by diluting an aqueous CNP90 colloidal solution with ethanol, a less polar solvent. The fluorescence intensity increased by approximately 1.5-fold compared with dilution in water, indicating that reducing solvent polarity enhances the fluorescence (Figure S24).

Moreover, we also evaluated the physically mixed T20/CNP90 nanofiber sample. Compared with pristine CNP90 nanofibers, it showed enhanced photoluminescence, a longer fluorescence lifetime, and improved photocatalytic activity (Figures S25–S27). However, these enhancements were less pronounced than those of the co-assembled T20/CNP90 sample, likely because T20 only partially and nonuniformly adsorbs onto the pre-formed CNP90 nanofibers through hydrophobic interactions. For the T80/CNP90 system, although the longer alkyl chains could generate a more densely packed hydrophobic interior with reduced internal water content, the excessive insulating alkyl chains may also hinder charge transport to the Pt co-catalysts, leading to slightly diminished photocatalytic activity for T80/CNP90.

Taken together, the introduction of amphiphilic surfactant T20 for nanoprecipitation exerts a profound influence on both the photophysical properties and photocatalytic performance of the molecular photocatalyst, as illustrated in Figure 5. Upon co-assembly, the hydrophilic polyoxyethylene chains of T20 extend toward the aqueous phase, enriching water concentrations at the catalyst surface and thereby increasing the availability of reactants for the hydrogen evolution reaction. Meanwhile, the hydrophobic hydrocarbon tail restricts water penetration into the nanofiber interior, suppressing nonradiative recombination losses in CNP90 and enabling more efficient utilization of photoexcited energy. In addition, the ordered assembly of D–A structured CNP90 molecules provides an efficient electron-transport channel, facilitating charge migration and accumulation. These synergistic effects collectively give rise to the exceptional photocatalytic hydrogen evolution rate observed for T20/CNP90.

3 | Conclusion

While surfactants are widely used in the synthesis of organic nanophotocatalysts, their fundamental roles at the photocatalyst–solution interface remain controversial and poorly understood. Here, we demonstrate that nanoprecipitation of D–A molecule CNP90 with the amphiphilic surfactant T20 not only improves colloidal stability and dispersion, but also profoundly modulates the photophysical properties of the nanophotocatalysts. Compared to bare CNP90, the T20/CNP90 exhibits largely enhanced photoluminescence quantum efficiency and charge generation. These synergistic gains translate into more than a 16-fold enhancement in the photocatalytic hydrogen evolution rate, reaching 520.17 mmol g^{-1} h^{-1}, which ranks among the highest reported for organic photocatalysts (Table S3). Importantly, this exceptional mass normalized activity is accompanied by high absolute hydrogen production (Figure 2e), overcoming a common limitation in nanophotocatalyst systems where high rates are often attained only under low catalyst loadings and thus limited overall output. Molecular dynamics simulations reveal that the

introduction of amphiphilic Tween restructures the interfacial microenvironment at the photocatalyst surface: its hydrophilic moieties form an outer hydration layer that increases the active sites for hydrogen evolution by adsorbing water, while its hydrophobic segments assemble into an inner shell that shields the nanophotocatalysts from polar water, thereby suppressing nonradiative recombination losses. Beyond providing fundamental insight, this work establishes a simple, cost-effective, and broadly applicable strategy for designing high-performance photocatalytic systems using ubiquitous surfactants.

4 | Experimental Section

4.1 | Synthesis of Compound 4-(2-Cyanoacetyl) Benzonitrile (a)

Sodium hydride (NaH, 60% dispersion in mineral oil, 497.7 mg, 12.4 mmol) was added to 100 mL of anhydrous acetonitrile. This mixture was stirred at room temperature for 15 min, and then 4-Cyano-benzoic acid methyl ester (1.0 g, 6.2 mmol) was added and reacted under N_2 at 60°C for 2 h. After cooling to room temperature, the mixture was poured into HCl (2 M) aqueous soliton and extracted with ethyl acetate (50 mL). The aqueous layer was further extracted with CH_2Cl_2 (3 × 50 mL). The combined organic layers were dried by anhydrous sodium sulfate and concentrated in rotary evaporator. After evaporation, the crude materials were subsequently purified by column chromatography using ethyl acetate as an eluent to afford a (592.6 mg, 56%) as a pale-yellow powder.

4.2 | Synthesis procedures for 2,6-bis(4-cyanophenyl)-4-(9-phenyl-9H-carbazol-3-yl) pyridine-3,5-dicarbonitrile (CNP90)

The CNP90 was synthesized using the Hantszch pyridine condensation reaction with modifications. A reaction flask was charged with a (3.0 mmol), 9-phenyl-9H-carbazole-3-carbaldehyde (b, 1.5 mmol), and ammonium acetate (7.5 mmol), then glacial acetic acid (15.0 mL) was added. The reaction mixture was heated to 110°C overnight. The result precipitates were filtered and washed with methanol. Then, the solids were oxidized with 2,3-dichloro-5,6-dicyano-*p*-benzoquinone (DDQ) in acetic acid solution at 110°C for 1 h, followed by filtration and washing with methanol. The solids were purified by column chromatography using petroleum ether/ethyl acetate as eluent, giving the final product as a yellow solid. ^{1}H NMR (400 MHz, DMSO-d_6): δ 8.80 (d, J = 1.8 Hz, 1 H), 8.33 (d, J = 7.7 Hz, 1 H), 8.32-8.20 (m, 4 H), 8.20-8.12 (m, 4 H), 7.93 (dd, J = 8.6, 1.9 Hz, 1 H), 7.74 (d, J = 5.8 Hz, 4 H), 7.66-7.58 (m, 2 H), 7.55 (ddd, J = 8.3, 7.1, 1.2 Hz, 1 H), 7.42 (dd, J = 16.2, 8.0 Hz, 2 H).

4.3 | Preparation of Nanophotocatalysts via Stirring Nanoprecipitation

For CNP90, 3 mL of the stock solution was added dropwise into a Tween (T20) aqueous solution (0.50 mg mL^{-1}) under continuous stirring (1000 rpm) for 2 min. The residual acetone was removed by heating the mixture in a water bath at 80°C, yielding a clear colloidal dispersion.

To evaluate the generality of the T20-assisted nanoprecipitation strategy, additional reported organic photocatalysts were prepared following the same protocol. NPI (1,8-naphthalimide), F8BT (poly(9,9-dioctylfluorene-alt-benzothiadiazole)), 4CzPN (3,4,5,6-tetra(9H-carbazol-9-yl)phthalonitrile), CNP8, CNP36, CNP90, CNP147 (pyridine-3,5-dicarbonitrile derivatives), and other small molecules were dissolved in acetone (0.50 mg mL^{-1}) as stock solutions prior to nanoprecipitation. $PC_{71}BM$ (0.50 mg mL^{-1} in acetone) emulsions were prepared by probe sonication for 30 min, followed by heating at 80°C to remove residual solvent.

4.4 | Flash Nanoprecipitation for Scaled-Up Production

For flash nanoprecipitation (FNP), CNP90 was dissolved in acetone (0.50 mg mL^{-1}) as the organic stream (stream 1). The solution was introduced into a multi-inlet vortex mixer (MIVM) together with three aqueous T20 streams (0.50 mg mL^{-1}; streams 2–4). Flow rates were set at 12 mL min^{-1} for streams 1 and 2 and 44 mL min^{-1} for streams 3 and 4 using digitally controlled syringe pumps (Harvard Apparatus, PHD 2000). The process yielded clear colloidal dispersions at ~25°C. Residual acetone was removed by heating at 80°C in a water bath to afford stable aqueous nanophotocatalyst dispersions.

4.5 | Photocatalytic Hydrogen Evolution Measurements

Photocatalytic hydrogen evolution experiments were conducted in an online glass system (Perfectlight-6A). Typically, a quartz reactor was charged with colloidal solution (25 mL) containing nanophotocatalysts, ascorbic acid, and a certain amount of Pt as a cocatalyst using hexachloroplatinic acid as a Pt precursor. The system was irradiated from the top using a 300 W xenon lamp (Perfectlight PLS-SXE300D) with different filters. The temperature of the reaction solution was maintained at 10°C by circulation of ethanol. The evolved gases were detected on a gas chromatograph (Shimadzu GC 2014C) with a thermal conductive detector.

Acknowledgements

This study is supported by National Natural Science Foundation of China (Nos. NSFC, 22422805, T2488302, 22521201, 22375062, 22338006 and 92356301); Guangxi Science and Technology Innovation Platform Program ("Leitai" Action Plan-Guangxi Laboratory Capacity Building, LT2504240035); the Scientific Research Innovation Capability Support Project for Young Faculty (ZYGXQNJSKYCXNLZCXM-M10); Shanghai Pilot Program for Basic Research (No. 22TQ1400100-10); the Science and Technology Commission of Shanghai Municipality (Nos. 24DX1400200 and 24160711900); Fundamental and Interdisciplinary Disciplines Breakthrough Plan of the Ministry of Education of China (No. JYB2025XDXM404); the Open Research Fund of State Key Laboratory of Precision and Intelligent Chemistry. We acknowledge the Research

Center of Analysis and Test of East China University of Science and Technology (ECUST) for assistance with various characterizations.

Conflicts of Interest

The authors declare no conflicts of interest.

Data Availability Statement

The data that supports the findings of this study are available in the supplementary material of this article.

References

1. T. Hisatomi, J. Kubota, and K. Domen, "Recent Advances in Semiconductors for Photocatalytic and Photoelectrochemical Water Splitting," *Chem Soc Rev* 43 (2014): 7520–7535.

2. K. Domen, A. Kudo, and T. Onishi, "Mechanism of Photocatalytic Decomposition of Water into H_2 and O_2 over NiO-$SrTiO_3$," *Journal of Catalysis* 102 (1986): 92–98.

3. N. S. Lewis and D. G. Nocera, "Powering the Planet: Chemical Challenges in Solar Energy Utilization," *Proceedings of the National Academy of Sciences* 103 (2006): 15729–15735.

4. Q. Wang and K. Domen, "Particulate Photocatalysts for Light-driven Water Splitting: Mechanisms, Challenges, and Design Strategies," *Chemical Reviews* 120 (2020): 919–985.

5. Y. Guo, Q. Zhou, B. Zhu, C. Y. Tang, and Y. Zhu, "Advances in Organic Semiconductors for Photocatalytic Hydrogen Evolution Reaction," *EES Catalysis* 1 (2023): 333–352.

6. Y. Fu, H. Liu, B. Z. Tang, and Z. Zhao, "Realizing Efficient Blue and Deep-blue Delayed Fluorescence Materials with Record-beating Electroluminescence Efficiencies of 43.4%," *Nature Communications* 14 (2023): 2019.

7. V. W. Lau, I. Moudrakovski, T. Botari, et al., "Rational Design of Carbon Nitride Photocatalysts by Identification of Cyanamide Defects as Catalytically Relevant Sites," *Nature Communications* 7 (2016): 12165.

8. S. Mathur, B. Rogers, and W. Wei, "Organic Conjugated Polymers and Polymer Dots as Photocatalysts for Hydrogen Production," *Frontiers in Energy* 15 (2021): 667–677.

9. Q. Li, J. N. Chang, Z. Wang, et al., "Modulated Connection Modes of Redox Units in Molecular Junction Covalent Organic Frameworks for Artificial Photosynthetic Overall Reaction," *Journal of the American Chemical Society* 145 (2023): 23167–23175.

10. L. Lin, Z. Lin, J. Zhang, et al., "Molecular-level Insights on the Reactive Facet of Carbon Nitride Single Crystals Photocatalysing Overall Water Splitting," *Nature Catalysis* 3 (2020): 649–655.

11. B. Cai, A. Brnovic, M. V. Pavliuk, et al., "Organic Crystalline Nanoparticles with a Long-Lived Charge-Separated State for Efficient Photocatalytic Hydrogen Production," *Nature Chemistry* 18 (2026): 723–730, https://doi.org/10.1038/s41557-025-02035-z.

12. X. Wang, K. Maeda, A. Thomas, et al., "A Metal-free Polymeric Photocatalyst for Hydrogen Production From Water Under Visible Light," *Nature Materials* 8 (2009): 76–80.

13. T. Banerjee, F. Haase, G. Savasci, K. Gottschling, C. Ochsenfeld, and B. V. Lotsch, "Single-site Photocatalytic H_2 Evolution From Covalent Organic Frameworks With Molecular Cobaloxime Co-Catalysts," *Journal of the American Chemical Society* 139 (2017): 16228–16234.

14. Y. Zhu, Z. Zhang, W. Si, et al., "Organic Photovoltaic Catalyst with Extended Exciton Diffusion for High-Performance Solar Hydrogen Evolution," *Journal of the American Chemical Society* 144 (2022): 12747–12755.

15. Y. Wang, A. Vogel, M. Sachs, et al., "Current Understanding and Challenges of Solar-Driven Hydrogen Generation Using Polymeric Photocatalysts," *Nature Energy* 4 (2019): 746–760.

16. S. Wang, Z. Ai, X. Niu, et al., "Linker Engineering of Sandwich-Structured Metal–Organic Framework Composites for Optimized Photocatalytic H_2 Production," *Advanced Materials* 35 (2023): 2302512.

17. F. Leng, H. Liu, M. Ding, Q.-P. Lin, and H.-L. Jiang, "Boosting Photocatalytic Hydrogen Production of Porphyrinic MOFs: the Metal Location in Metalloporphyrin Matters," *ACS Catalysis* 8 (2018): 4583–4590.

18. J. Zhang, X. Liang, C. Zhang, et al., "Improved Charge Separation in Poly(heptazine-triazine) Imides with Semi-Coherent Interfaces for Photocatalytic Hydrogen Evolution," *Angewandte Chemie International Edition* 61 (2022): 202210849.

19. Y. Wang, P. Maity, Z. Liu, et al., "Boosted Hydrogen Evolution via Photoinduced Hole Transfer in Molecular-Level Organic Heterojunction under NIR Photon Excitation," *Advanced Materials* 37 (2025): 2415161.

20. S. A. J. Hillman, R. S. Sprick, D. Pearce, et al., "Why Do Sulfone-containing Polymer Photocatalysts Work so Well for Sacrificial Hydrogen Evolution from Water?," *Journal of the American Chemical Society* 144 (2022): 19382–19395.

21. R. S. Sprick, J. X. Jiang, B. Bonillo, et al., "Tunable Organic Photocatalysts for Visible-Light-Driven Hydrogen Evolution," *Journal of the American Chemical Society* 137 (2015): 3265–3270.

22. I. McCulloch, M. Heeney, C. Bailey, et al., "Liquid-Crystalline Semiconducting Polymers With High Charge-Carrier Mobility," *Nature Materials* 5 (2006): 328–333.

23. R. Noriega, J. Rivnay, K. Vandewal, et al., "A General Relationship Between Disorder, Aggregation and Charge Transport in Conjugated Polymers," *Nature Materials* 12 (2013): 1038–1044.

24. Y. Chen, S. Ji, Y. Wang, et al., "Isolated Single Iron Atoms Anchored on N-Doped Porous Carbon as an Efficient Electrocatalyst for the Oxygen Reduction Reaction," *Angewandte Chemie International Edition* 56 (2017): 6937–6941.

25. X. Wang, L. Chen, S. Y. Chong, et al., "Sulfone-containing Covalent Organic Frameworks for Photocatalytic Hydrogen Evolution from Water," *Nature Chemistry* 10 (2018): 1180–1189.

26. Y. Wang, P. Maity, Y. Jia, et al., "Intrinsically Charge-generating Polymers with Long-lived Free Carriers for Efficient Photon-to-hydrogen Conversion," *Science Advances* 11 (2025): aea4191.

27. Y. Yang, M. A. Zwijnenburg, A. M. Gardner, et al., "Conjugated Polymer/Recombinant escherichia coli Biohybrid Systems for Photobiocatalytic Hydrogen Production," *ACS Nano* 18 (2024): 13484–13495.

28. C. Shu, C. Han, X. Yang, et al., "Boosting the Photocatalytic Hydrogen Evolution Activity for D–π–A Conjugated Microporous Polymers by Statistical Copolymerization," *Advanced Materials* 33 (2021): 2008498.

29. Y. Tamai, H. Ohkita, H. Benten, and S. Ito, "Exciton Diffusion in Conjugated Polymers: from Fundamental Understanding to Improvement in Photovoltaic Conversion Efficiency," *The Journal of Physical Chemistry Letters* 6 (2015): 3417–3428.

30. Y. Li, D. Cheng, J. Tian, et al., "Unlocking High Lithium-ion Transport in Solid Polymer Electrolytes with Dynamic Hydrogen-bonded Zinc-adeninate Framework," *Cell Reports Physical Science* 6 (2025): 102624.

31. H. Qiu, Z. M. Hudson, M. A. Winnik, and I. Manners, "Multidimensional Hierarchical Self-assembly of Amphiphilic Cylindrical Block Comicelles," *Science* 347 (2015): 1329–1332.

32. H. Qiu, Y. Gao, V. A. Du, R. Harniman, M. A. Winnik, and I. Manners, "Branched Micelles by Living Crystallization-Driven Block Copolymer Self-assembly under Kinetic Control," *Journal of the American Chemical Society* 137 (2015): 2375–2385.

33. J. Cerda, S. Giannini, L. Xu, L. Wang, and D. Beljonne, "Tuning Exciton Diffusion in Organic Semiconductors through Hybridization With Charge-Transfer Excitations," *The Journal of Physical Chemistry Letters* 16 (2025): 8673–8682.

34. L. Zhu, M. Zhang, J. Xu, et al., "Single-junction Organic Solar Cells with over 19% Efficiency Enabled by a Refined Double-Fibril Network Morphology," *Nature Materials* 21 (2022): 656–663.

35. Z. A. Lan, G. Zhang, X. Chen, Y. Zhang, K. A. I. Zhang, and X. Wang, "Reducing the Exciton Binding Energy of Donor–Acceptor-Based Conjugated Polymers to Promote Charge-Induced Reactions," *Angewandte Chemie International Edition* 58 (2019): 10236–10240.

36. J. Liu, Y. Liu, N. Liu, et al., "Metal-free Efficient Photocatalyst for Stable Visible Water Splitting via a Two-Electron Pathway," *Science* 347 (2015): 970–974.

37. C. Franco, D. Rodriguez-San-Miguel, A. Sorrenti, et al., "Biomimetic Synthesis of Sub-20 Nm Covalent Organic Frameworks in Water," *Journal of the American Chemical Society* 142 (2020): 3540–3547.

38. H. Yang, C. Li, T. Liu, et al., "Packing-induced Selectivity Switching in Molecular Nanoparticle Photocatalysts for Hydrogen and Hydrogen Peroxide Production," *Nature Nanotechnology* 18 (2023): 307–315.

39. W. Zhang, M. Yu, T. Liu, et al., "Accelerated Discovery of Molecular Nanojunction Photocatalysts for Hydrogen Evolution by Using Automated Screening and Flow Synthesis," *Nature Synthesis* 3 (2024): 595–605.

40. X. Liu, M. Yu, K. Huang, et al., "Efficient Quasi-Homogenous Photocatalysis Enabled by Molecular Nanophotocatalysts with Donor-Acceptor Motif," *Advanced Materials* 37 (2025): 2413440.

41. M. Yu, W. Zhang, Z. Guo, Y. Wu, and W. Zhu, "Engineering Nanoparticulate Organic Photocatalysts via a Scalable Flash Nanoprecipitation Process for Efficient Hydrogen Production," *Angewandte Chemie International Edition* 60 (2021): 15590–15597.

42. W. Zhao, L. Luo, M. Cong, et al., "Nanoscale Covalent Organic Frameworks for Enhanced Photocatalytic Hydrogen Production," *Nature Communications* 15 (2024): 6482.

43. B. Gui, X. Liu, Y. Cheng, et al., "Tailoring the Pore Surface of 3D Covalent Organic Frameworks via Post-Synthetic Click Chemistry," *Angewandte Chemie International Edition* 61 (2022): 202113852.

44. C. L. Chang, W. C. Lin, L. Y. Ting, et al., "Main-chain Engineering of Polymer Photocatalysts With Hydrophilic Non-Conjugated Segments for Visible-Light-Driven Hydrogen Evolution," *Nature Communications* 13 (2022): 5460.

45. M. Sachs, R. S. Sprick, D. Pearce, et al., "Understanding Structure-Activity Relationships in Linear Polymer Photocatalysts for Hydrogen Evolution," *Nature Communications* 9 (2018): 4968.

46. W. Zhao, Q. Zhu, X. Wu, and D. Zhao, "The Development of Catalysts and Auxiliaries for the Synthesis of Covalent Organic Frameworks," *Chemical Society Reviews* 53 (2024): 7531–7565.

47. J. Kosco, M. Bidwell, H. Cha, et al., "Enhanced Photocatalytic Hydrogen Evolution from Organic Semiconductor Heterojunction Nanoparticles," *Nature Materials* 19 (2020): 559–565.

48. J. Kosco, S. Gonzalez-Carrero, C. T. Howells, et al., "Generation of Long-lived Charges in Organic Semiconductor Heterojunction Nanoparticles for Efficient Photocatalytic Hydrogen Evolution," *Nature Energy* 7 (2022): 340–351.

49. Y. Ma, S. Yu, W. Li, et al., "Rapid yet Controlled Synthesis of 2D Covalent Organic Framework Nanocapsules as High-Performance Photocatalytic Carriers," *Angewandte Chemie International Edition* 64 (2025): 202416980.

50. W. C. Lin, Y. E. Sun, Y. R. Zhuang, et al., "Optimally Miscible Polymer Bulk-Heterojunction-Particles for Nonsurfactant Photocatalytic Hydrogen Evolution," *Journal of the American Chemical Society* 147 (2025): 2537–2548.

51. J. Bruder, K. Fischer, J. Armleder, et al., "Photocatalytic Hydrogen Generation in Surfactant-Free, Aqueous Organic Nanoparticle Dispersions," *Small* 20 (2024): 2406236.

52. M. H. Elsayed, M. Abdellah, A. Z. Alhakemy, et al., "Overcoming Small-bandgap Charge Recombination in Visible and Nir-light-driven Hydrogen Evolution by Engineering the Polymer Photocatalyst Structure," *Nature Communications* 15 (2024): 707.

53. H. Hou, Y. X. Ma, B. T. Liu, X. Chen, and Y. Zhao, "Microporous Confinement of One-dimensional Covalent Organic Frameworks for Surface-regulated Photocatalytic Hydrogen Evolution," *Journal of the American Chemical Society* 148 (2026): 20940–20950, https://doi.org/10.1021/jacs.6c05080.

54. Z. S. Zhu, S. Zhong, C. Cheng, et al., "Microenvironment Engineering of Heterogeneous Catalysts for Liquid-Phase Environmental Catalysis," *Chemical Reviews* 124 (2024): 11348–11434.

55. C. Xu, R. Ye, H. Shen, J. W. Y. Lam, Z. Zhao, and B. Z. Tang, "Molecular Motion and Nonradiative Decay: Towards Efficient Photothermal and Photoacoustic Systems," *Angewandte Chemie International Edition* 61 (2022): 202204604.

56. M. Z. Rahman and C. B. Mullins, "Understanding Charge Transport in Carbon Nitride for Enhanced Photocatalytic Solar Fuel Production," *Accounts of Chemical Research* 52 (2019): 248–257.

57. E. M. Kosower, H. Dodiuk, and H. Kanety, "Intramolecular Donor-acceptor System. 4. Solvent Effects on Radiative and Nonradiative Processes for the Charge-transfer States of N-Arylaminonaphthalenesulfonates," *Journal of the American Chemical Society* 100 (1978): 4179–4188.

58. J. Maillard, K. Klehs, C. Rumble, E. Vauthey, M. Heilemann, and A. Furstenberg, "Universal Quenching of Common Fluorescent Probes by Water and Alcohols," *Chemical Science* 12 (2020): 1352–1362.

59. B. Dereka and E. Vauthey, "Direct Local Solvent Probing by Transient Infrared Spectroscopy Reveals the Mechanism of Hydrogen-bond Induced Nonradiative Deactivation," *Chemical Science* 8 (2017): 5057–5066.

60. B. Dereka and E. Vauthey, "Solute–Solvent Interactions and Excited-State Symmetry Breaking: Beyond the Dipole–Dipole and the Hydrogen-Bond Interactions," *The Journal of Physical Chemistry Letters* 8 (2017): 3927–3932.

Supporting Information

Additional supporting information can be found online in the Supporting Information section.

Supporting File: adma73981-sup-0001-SuppMat.pdf.